Research in Diagnostic and Interventional Imaging 10 (2024) 100046

Contents lists available at ScienceDirect

Research in Diagnostic and Interventional Imaging

journal homepage: https://www.journals.elsevier.com/redii

Original article

Assessment of a multivariable model using MRI-radiomics, age and sex for the classification of hepatocellular adenoma subtypes

Guillaume Declaux[a], Baudouin Denis de Senneville[b,*], Hervé Trillaud[a,b], Paulette Bioulac-Sage[c,d], Charles Balabaud[d,e], Jean-Frédéric Blanc[e], Laurent Facq[b], Nora Frulio[a]

[a] Service d'imagerie diagnostique et Interventionnelle, centre médicochirurgical Magellan, hôpital Saint-André, centre hospitalier universitaire de Bordeaux, 33000, Bordeaux, France
[b] Université de Bordeaux, CNRS, Inria, Bordeaux INP, IMB, UMR 5251, 33400, Talence, France
[c] Service de pathologie, hôpital Pellegrin, centre hospitalier universitaire de Bordeaux, Bordeaux, France
[d] Université de Bordeaux, Bordeaux Research in Translational Oncology, Bordeaux, France
[e] Service d'hépato-gastroentérologie et oncologie digestive, centre médicochirurgical Magellan, hôpital Haut-Lévêque, centre hospitalier universitaire de Bordeaux, Bordeaux, France

ARTICLE INFO

Article History:
Received 7 November 2023
Accepted 1 April 2024
Available online 5 April 2024

Keywords:
Adenoma
Hepatocellular
Biomarker

ABSTRACT

Objectives: Non-invasive subtyping of hepatocellular adenomas (HCA) remains challenging for several subtypes, thus carrying different levels of risks and management. The goal of this study is to devise a multivariable diagnostic model based on basic clinical features (age and sex) combined with MRI-radiomics and to evaluate its diagnostic performance.

Methods: This single-center retrospective case-control study included all consecutive patients with HCA identified within the pathological database from our institution from January 2003 to April 2018 with MRI examination (T2, T1-no injection/injection-arterial-portal); volumes of interest were manually delineated in adenomas and 38 textural features were extracted (LIFEx, v5.10). Qualitative (i.e., visual on MRI) and automatic (computer-assisted) analysis were compared. The prognostic scores of a multivariable diagnostic model based on basic clinical features (age and sex) combined with MRI-radiomics (tumor volume and texture features) were assessed using a cross-validated Random Forest algorithm.

Results: Via visual MR-analysis, HCA subgroups could be classified with balanced accuracies of 80.8 % (I-HCA or ß-I-HCA, the two being indistinguishable), 81.8 % (H-HCA) and 74.4 % (sh-HCA or ß-HCA also indistinguishable). Using a model including age, sex, volume and texture variables, HCA subgroups were predicted (multivariate classification) with an averaged balanced accuracy of 58.6 %, best=73.8 % (sh-HCA) and 71.9 % (ß-HCA). I-HCA and ß-I-HCA could be also distinguished (binary classification) with a balanced accuracy of 73 %.

Conclusion: Multiple HCA subtyping could be improved using machine-learning algorithms including two clinical features, i.e., age and sex, combined with MRI-radiomics. Future HCA studies enrolling more patients will further test the validity of the model.

1. Introduction

Hepatocellular adenomas (HCA) are rare, benign liver tumors, with an incidence reported between 1/100,000 and 4/100,000 [1]. Frequently diagnosed in women in their reproductive age and with a women:men ratio of 10:1, these hormone-driven tumors typically develop in the setting of a hormonal or metabolic abnormality, such as long-term use of oral contraceptive pills, androgen exposure or obesity [2–4]. Complications, such as hemorrhage (15–20 %) or malignant transformation (5 %), were observed to increase with tumor size, leading to the recommendation to resect all HCA larger than 5 cm and all HCA detected in male

Abbreviations and acronyms: ß-HCA, ß-catenin hepatocellular adenoma; ß-I-HCA, ß-catenin inflammatory hepatocellular adenoma; BMI, body mass index; CF, clinical features; GRE, gradient echo; HCA, Hepatocellular adenomas; H-HCA, HNF1α mutated hepatocellular adenoma; HNF1α, hepatocyte nuclear factor 1α; I-HCA, Inflammatory hepatocellular adenoma; IRB, Institutional Review Board; MRI, magnetic resonance imaging; OC, oral contraceptive; PCA, Principal Component Analysis; TF, Texture features; sh-HCA, Sonic-Hedgehog hepatocellular adenoma; T1w, T1-weighted; T2w, T2-weighted; VF, volume features; VOI, volume of interest

* Corresponding author.
E-mail address: bdenisde@math.u-bordeaux.fr (B. Denis de Senneville).

https://doi.org/10.1016/j.redii.2024.100046

patients [5,6]. In other cases, the identification of the adenoma subtype is a key step in the management of adenoma. HCA encompass various monoclonal hepatocellular proliferations that can be classified into subtypes strongly associated with risk factors, clinical features and complications, but also their histological, immunohistochemical and radiologic hallmarks [7–12]. These subtypes are HNF1α adenomas (H-HCA), inflammatory adenomas (I-HCA), ß-catenin adenomas (ß-HCA), ß-catenin-inflammatory adenomas (ß-I-HCA) and Sonic-Hedgehog adenomas (sh-HCA). From the radiologic hallmarks, only 11.6 % of H-HCA and 12 % of I-HCA remain undiagnosed in the best series [9]. Recently, the hepatospecific contrast uptake in the hepatobiliary phase was discovered to be strongly associated with marked activation of the β-catenin pathway [13].

Despite the accuracy of these criteria, MRI fails to classify subtypes in other situations, in particular for the identification of ß-HCA and sh-HCA, but also the discrimination between ß-I-HCA and I-HCA [14]; anatomopathology including immunohistochemistry, molecular analysis, and more recently, proteomic analysis, allows this identification. This method requires a liver biopsy with a risk of bleeding recently reported to be 7 % in a large cohort [15].

The identification of adenoma subtypes in a non-invasive fashion remains a challenge because it is a key step in their management, either surgical, surveillance, or abstention; this holds especially true for adenomas displaying inflammatory phenotypes, sometimes ß-catenin mutated. Because of the rarity of adenomas, MRI series have small numbers of patients, so the chosen method must be adapted to small numbers. Hence, the diagnostic model devised in this study integrates two basic clinical features, namely age and sex, combined with MRI-based radiomic features (including tumor volume and texture features) and its performance to distinguish hepatocellular subtypes is tested. The purpose was to compare, as a preliminary study, the original concept of computer-assisted method with the usual qualitative (visual) analysis for the diagnosis of adenomas. To the best of our knowledge, no study has yet assessed the potential usefulness of MRI-radiomics features to aid adenoma classification.

2. Materials and methods

2.1. Study design and population

From January 2003 to April 2018, all consecutive patients with at least one confirmed HCA on liver specimen were retrospectively identified within our pathological database from our institution and affiliated hospitals (Fig. 1). Patients with the HCA subtypes H-HCA, I-HCA, ß-HCA, ß-I-HCA and sh-HCA were included. This single-center observational study was approved by the Institutional Review Board (IRB number CRM-2103-143). Informed consent was waived due to its retrospective nature.

2.2. Histological analysis

To classify HCA, the histological analysis on all tissue specimens was performed by two experienced readers who were blinded to clinical and radiological data. Subtyping of the surgical parts was performed by immunohistochemistry and molecular analysis, and only immunohistochemistry for the biopsy samples. When molecular analysis could not be performed due to a sample alteration, proteome analysis was performed [11]. Any adenoma without its own histological evidence was excluded from the analysis.

2.3. Clinical features

Clinical features of patients were retrospectively collected from our institution records when available: while age and sex were included in our study, BMIs, which were not known in all patients, were not included.

2.4. MRI protocols

From 2003 to 2018, each patient underwent a liver-MRI, either in our center or outside. For each patient, four MR-images were collected: one T2 weighted image without fat-signal suppression and three T1-weighted gradient echo images (T1w GRE) with in phase

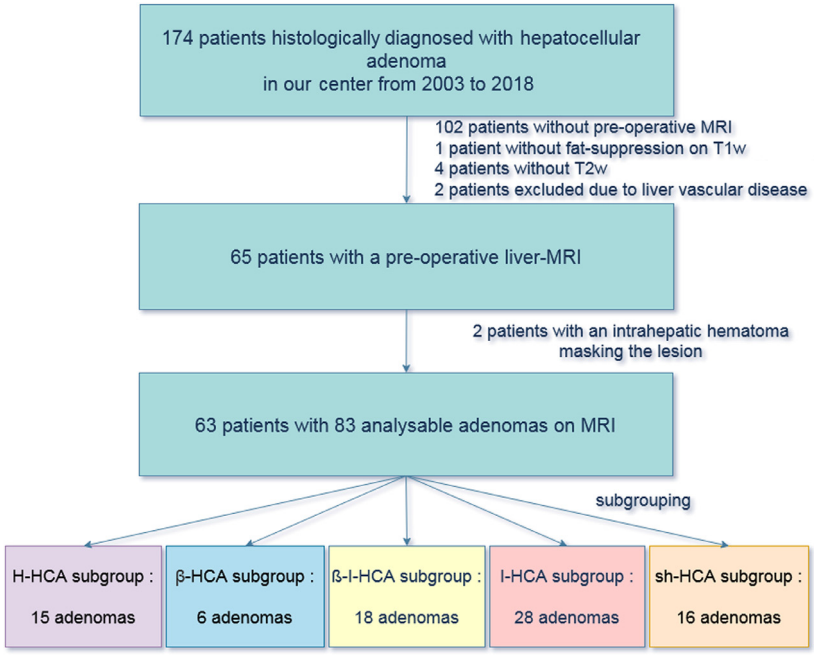

Fig. 1. Flowchart and study design.

and out phase chemicals shift (one image) and after (two images) intravenous injection of gadolinium-based contrast medium (pre-contrast phase/arterial phase at 30–40 s/portal phase at 90–120 s). MRI models are summarized in supplementary material.

2.5. MRI visual analysis

All MRI data were assessed retrospectively and independently in consensus by two abdominal radiologists NF, HT (more than 15 years experience), blinded to pathologic, clinical, and biological data. Each lesion was classified using pre-defined criteria. The sign associated with the subgroup of H-HCAs is a signal dropout on chemical shift sequences, assessing the presence of fatty hepatocytes. This signal dropout is diffuse and homogeneous [11]. The sign associated with the subgroup of I-HCA is related to sinusoidal dilatation with marked hyperintensity on T2W and persistent delayed enhancement translating global sinusoidal dilatation [11,12] or complete hyperintense peripheral rim on T2W, typically enhanced in the late vascular phase, with isointense and homogenous center similar to surrounding liver, known as the atoll sign. Lesions without these signs were HCA without visual identification of the subtype, grouping ß-HCA and sh-HCA. Visual discrimination between I-HCA and ß-I-HCA could not be achieved in our daily practice unless resorting to hepatospecific contrast medium. Hence, I-HCA and ß-I-HCA were here merged into a new subgroup referred to as "(ß-)I-HCA".

2.6. MRI data processing

Slice-by-slice delineation of a volume of interest (VOI) was performed manually (freehand) for each tumor by a resident in Radiology using LIFEx freeware (version 5.10, Inserm, Orsay, France, www.lifexsoft.org) [16].

Prior to feature extraction, additional image spatial harmonization and standardization was conducted to avoid inhomogeneity, as indicated by Masson et al. [17]. For each image, the intensity range was normalized by means of Z-scoring [mean +/- 3 SD]. Image intensities were discretized into 128 fixed bins.

2.7. MRI-radiomics feature extraction

The entire tumor volume was used during image manual delineation and texture analysis (Fig. 2). The presence of hemorrhagic remodeling masking the tumor tissue resulted in dataset exclusion; in case of hemorrhagic changes not masking the tumor, the tumor tissue was segmented, but not the hematoma.

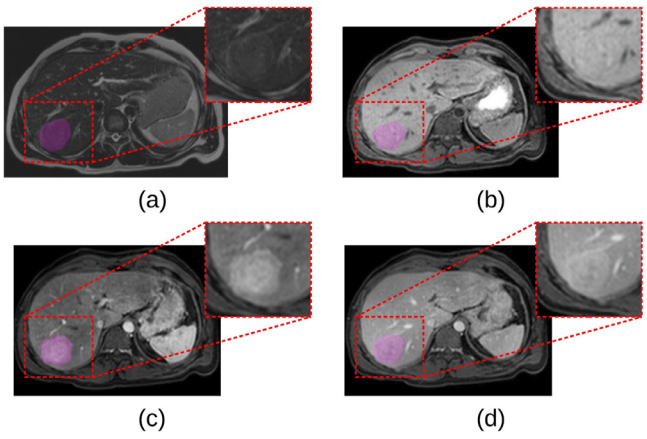

Fig. 2. Representative MR-images of a ß-I-HCA of the segment VII obtained using a T2w sequence (a), a T1w sequence before (b) and after injection at arterial phase (c) and portal phase (d). The adenoma is manually segmented in 3 dimensions (purple region). The adenoma is emphasized in each insert.

Using each of the four above-mentioned MRI protocols, the tumor volume and a total of 38 textural radiomics features (TF) were calculated from each VOI using the above-mentioned LIFEx freeware [16] including: 6 histogram-based features and 32 s-order texture features from gray-level co-occurrence matrix (GLCM, N = 7, with a 1-voxel distance to neighbors), gray-level run length matrix (GLRLM, N = 11), neighborhood gray-level different matrix (NGLDM, N = 3), and gray-level zone length matrix (GLZLM, N = 11). TFs were individually centered (by removing the training mean) and scaled (to unit variance) beforehand. As underlined by Jolliffe et al. [18], sufficiently large patient cohorts are required to avoid under powering and "noise discovery"; ten patients per individual predictor investigated may be advised. TF with P-value < 0.05 with Bonferroni correction were selected (analysis of variance (ANOVA) for multi-variate classification/Mann Whitney for binary classification/all TFs selected in default). A Principal component analysis (PCA) was then applied to create a single combined TF variable in order to reduce dimensionality of selected TF-features while preserving its information, as suggested by Halligan et al. [19].

2.8. MRI automatic analysis

The diagnostic performances of a multivariable model including four categorical variables (2 clinical features: Age, Sex; and 2 radiomics features: tumor Volume and Texture) as inputs (this model is denoted by "ASVT model"). The diagnostic performances are compared to the following two classification models:

1. A univariable model (denoted by "VF model") including the volume feature as an input.
2. A multivariable model (denoted by "ASV model") including three categorical variables – Age, Sex and Volume – as inputs.

The automatic classifiers were evaluated for multi-variate (5 classes: H-HCA, I-HCA, ß-HCA, ß-I-HCA and sh-HCA) and binary (2 classes: I-HCA and ß-I-HCA) classifications.

2.9. Statistical analysis

The analysis was conducted with the commercial software MATLAB (©1994–2022 The MathWorks, Inc./Statistics and Machine Learning toolbox). The classifier was the Random Forest machine-learning algorithm (default hyperparameters in the MATLAB implementation). The diagnostic performance of the automatic classifiers was evaluated through cross-validation [20,21] (90 % patients training/10 % testing, ensuring that all HCA subtypes to classify are present in both training and testing datasets, 1000 trials with random shuffling). The balanced accuracies, sensitivity, specificity, positive predictive values (PPVs) and negative predictive values (NPVs) of qualitative (visual) and automatic (computer-assisted) analyses were recorded. For automatic analyses, area under the ROC curve (AUROC) was also computed.

3. Results

3.1. Demographic characteristics

The study included 174 patients based on pathological results; 107 patients without preoperative MRI or without adequate MRI data (102 had no MRI, 5 had MRIs without the required sequences) were excluded. Four patients were further excluded because of lesion hemorrhage masking the tumor tissue for two and with hepatic vascular disease for two. Seventeen patients presented multiple adenomas: only one patient exhibited two different subtypes (i.e., ß-I-HCA

Table 1
Demographic characteristics and phenotype correlation according to HCA subgroups. The P-value of an analysis of variance (ANOVA) is provided for categorical variable available in all patients (top right column, NA=Not Applicable).

	Total	Sonic-Hedgehog HCA (sh-HCA)	Inflammatory HCA (I-HCA)	ß-catenin-inflammatory HCA (ß-I-HCA)	ß-catenin- HCA (ß-HCA)	HNF1α HCA (H-HCA)	P-value (ANOVA)
# of patients	63	13	17	14	6	13	NA
Age [year] median (min-max)	38 (21–61)	40.5	38	36.5	31	36	0.032
# of women:men	53:10	13:0	15:2	10:4	6:0	9:4	0.252
Women: children?							NA
Yes [# (mean)]	19 (2.1)	5 (1.6)	6 (2.3)	3 (3)	3 (1.7)	/	
No	14	5	5	3	1	/	
Not available	13	3	4	4	2	9	
Women: OCP intake history?							NA
Yes	35	11	13	8	3	/	
No	2	0	1	1	0	/	
Not available	7	2	1	1	3	9	
BMI [kg/m^2] mean (range)*	28.9 (19–45)	32.6	28.1	25.1	29	/	NA
Diabetes	5	4	1	0	0	/	NA
Revelation mode	56	12	14	13	5	12	NA
Chance	17	2	7	3	0	5	NA
Liver biology abnormalities	7	0	4	1	1	1	NA
Pain	23	6	3	9	0	5	NA
Bleeding	8	4	0	0	3	1	NA
Inflammatory syndrome	0	0	0	0	0	0	NA
Other: eclampsia	1	0	0	0	1	0	NA
# of HCA on MRI							0.023
1	46	9	10	10	6	11	
[2–4]	12	3	5	3	0	1	
[5–10]	3	1	1	1	0	0	
>10	2	0	1	0	0	1	
Size of lesion [mm] median (range)**	47 (12–162)	60,5 (28–138)	38 (12–144)	50 (13–100)	108 (43–162)	56 (23–133)	0.001

* BMI was available in 34 out of 63 patients.
** Largest axis in the axial plane.

and I-HCA), while the remaining 16 patients had the same subtype (Fig. 1 and Table 1).

A total of 83 HCA from 63 patients were thus analyzed. Tissue specimens were obtained from surgical specimens in 77 cases and biopsies in 6 cases. Of the six patients where liver biopsies were collected, three had curative treatments by interventional radiology and three were followed-up by MRI. The clinical and histological features were similar to those reported in series of resected HCA (Table 1).

3.2. Statistical analysis

Via visual MR-analysis, HCA subgroups could be classified with balanced accuracies of 80.8 % (I-HCA or ß-I-HCA, the two being indistinguishable), 81.8 % (H-HCA) and 74.4 % (sh-HCA and ß-HCA) (Table 2).

Via automatic (computer-assisted) analyses, HCA subgroups were predicted (multi-variate classification) with a balanced accuracy of 58.6 % (averaged over the 5 subgroups) using the multivariable model including four variables age, sex, volume and texture (ASVT model/T2 no fat saturation MRI) (Table 3). Using this model, best balanced accuracies were 73.8 % (sh-HCA) and 71.9 % (ß-HCA) (H-HCA) (Table 4).

For the binary classification of inflammatory groups (I-HCA and ß-I-HCA), the ASVT model provided a balanced accuracy of 73 % and AUROC of 0.71 using a T1-no injection MRI (Table 5).

4. Discussion

The advent of artificial intelligence for radiological applications holds great promise for the development of novel diagnostic approaches such as radiomics. Tumor volume calculated from manual delineation on MRI combined with the texture variable and two basic patient identifiers, i.e., age and sex, allowed subgrouping inflammatory HCA non-invasively with a balanced accuracy of 73 % and an AUROC of 0.71. In our opinion, this result is the most interesting of this study because ß-I-HCA and I-HCA have a different therapeutic management, invasive or non-invasive, in spite of their common inflammatory features, thus making the ASVT model particularly valuable.

Although showing some efficiency in subtyping the five analyzed HCA subgroups, the use of the ASVT model provided in average modest classification scores (balanced accuracy $\sim$ 58.6 % using the ASVT model/T2 no fat saturation sequence). Interestingly, the ASVT model

Table 2
Qualitative (i.e., visual on MRI) scores obtained for each adenoma subgroup. Visual discrimination between I-HCA and ß-I-HCA could not be achieved in our daily practice unless resorting to hepatospecific contrast medium. Hence, I-HCA and ß-I-HCA were here merged into a subgroup referred to as "(ß-)I-HCA" (31 patients, 46 tumors). Moreover, ß-HCA could never be identified visually. Hence, ß-HCA and sh-HCA were here merged into a subgroup referred to as "No visual identification of the subtype" (19 patients, 22 tumors). Balanced accuracies, sensitivities, specificities, PPVs, and NPVs are shown in percentages.

Adenoma subgroups	Tumor number (#)	Balanced accuracy (%)	Sensitivity (%)	Specificity (%)	PPV (%)	NPV (%)
(ß-)I-HCA	46	80.8	80.9	80.6	86.4	73.5
H-HCA	15	81.8	66.7	96.8	83.3	92.4
No visual identification of the subtype	22	74.4	68.2	80.6	55.6	87.7

Table 3
Diagnostic performance obtained by the implemented automatic classifiers for HCA subtyping (multivariate classification/5 classes: sh-HCA, I-HCA, ß-I-HCA, ß-HCA and H-HCA). Classification results are reported after cross-validation (90 % patients training/10 % testing, all subtypes present in both training and testing datasets, 1000 trials with random shuffling) by the Random Forest algorithm. VF: univariable model including the lesion volume feature, TF: univariable model including the texture feature, ASV: multivariable model including three variables (age, sex and volume), ASVT: multivariable model including four variables (age, sex, volume and texture). Balanced accuracy, area under the ROC curve (AUROC), sensitivity, specificity, positive predictive value (PPV) and negative predictive values (NPV) were recorded. Averages over adenoma subgroups of the tested metrics are reported. Top-scores (i.e., highest balanced accuracy) are highlighted in bold characters.

Multivariate classification (5 classes: sh-HCA/I-HCA/ß-I-HCA/ß-HCA/H-HCA)						
Classifier	Balanced accuracy (%)	AUROC	Sensitivity (%)	Specificity (%)	PPV (%)	NPV (%)
VF model (volume feature)						
T2 no fat saturation	55.2	0.55	27.7	82.7	20.9	83.4
T1 no injection	54.9	0.55	27.2	82.6	20.3	83.2
T1 arterial	55.9	0.56	28.8	83.0	21.8	83.7
T1 portal	54.8	0.55	27.1	82.5	20.0	83.1
ASV model (age, sex and volume features)						
T2 no fat saturation	52.0	0.51	23.9	80.2	16.7	80.4
T1 no injection	51.7	0.50	23.3	80.0	15.9	80.1
T1 arterial	51.5	0.49	23.1	79.9	15.8	80.0
T1 portal	51.5	0.50	22.9	80.0	16.0	80.0
ASVT model (age, sex, volume and texture features)						
T2 no fat saturation	**58.6**	**0.59**	**34.5**	**82.6**	**28.9**	**82.7**
T1 no injection	54.7	0.59	28.3	81.1	21.0	81.5
T1 arterial	53.2	0.56	25.6	80.8	18.4	81.0
T1 portal	55.3	0.57	29.5	81.2	22.8	81.2

was found to have a clear benefit for sh-HCA and ß-catenin. Hence, sh-HCA and ß-HCA could be distinguished from with a balanced accuracy of 73.8 % and 71.9 %, respectively, a discrimination that could not be achieved in our daily practice with qualitative visual analysis unless resorting to hepatospecific contrast medium.

To date, the present study has, to the best of our knowledge, one of the largest collections of HCA MRI data where all HCA are histologically documented. On top of that, all surgical specimens were examined by experts (radiologist and pathologist) according to the state of the art in their respective field, and updated if necessary; it is worth noting that such updates are essential to avoid biases induced by the evolution of knowledge in pathology throughout the recruitment period, which started in 2003.

Our study has some limitations worth mentioning; lower scores were obtained for the ß-HCA subgroup owing to the lack of patient data for such a subtype. Moreover, the ß-catenin subgroups could not be split according to the location of the ß-catenin gene mutation (exon 3 or exons 7–8) because of the lack of patient data for such categories. In addition, patients' BMIs were not included in the analysis because this information was incomplete in the patients' data. Furthermore, our analysis did not encompass MRI data obtained from diffusion imaging and fat saturation on T2w sequences because of insufficient data in our database; for the same reason, gadoxetic acid-enhanced MRI data for the analysis of the hepato-biliary phase could not be included in the present study. Nonetheless, such data are of particular relevance: diffusion radiomics has been shown to distinguish HCA from benign hepatic nodules [22]; the T2w sequence with fat saturation is known to provide a better liver-to-lesion contrast; last, intracellular contrast media exhibited specific characteristics on hepatobiliary-phase, especially for exon3-mutated ß-catenin HCA [23,24].

Overall, our results indicate that automatic (computer-assisted) approach could have the clear potential to be added to the diagnostic arsenal of adenomas subtypes in the near future, thus giving an increasing importance to non-invasive techniques over invasive procedures with their substantial shortcomings, such as bleeding risks and costs related to the biopsy procedure.. In this study, automatic classifiers were potentially suitable for the subtyping of small tumors, i.e., smaller than 5 cm, usually considered being difficult cases. Given the numerous challenges associated with MRI-automatic analysis [25], the validity of our approach will be confirmed in future studies, preferably prospective ones, involving larger patient cohorts.

Table 4
Diagnostic performance of the top-predictive classifier (ASVT model/T2 no fat saturation) for the prediction of each HCA subgroup (multivariate classification/5 classes: sh-HCA, I-HCA, ß-I-HCA, ß-HCA and H-HCA). Averages of the tested metrics (balanced accuracies, AUROC, sensitivity, specificity, PPV and NPV) were calculated with standard deviations and 95 % confidence intervals. Balanced accuracies, sensitivities, specificities, PPVs, and NPVs are shown in percentages.

Adenoma subgroups	Tumor number (#)	Balanced accuracy (%)	AUROC	Sensitivity (%)	Specificity (%)	PPV (%)	NPV (%)
sh-HCA	16	73.8 ± 22.7 (72.4 −75.2)	0.70 ± 0.34 (0.67 −0.72)	57.9 ± 44.9 (55.1 −60.7)	89.6 ± 14.7 (88.7 −90.6)	50.6 ± 43.3 (47.9 −53.3)	89.4 ± 12.1 (88.6 −90.1)
I-HCA	28	45.2 ± 21.4 (43.9 −46.5)	0.44 ± 0.26 (0.43 −0.46)	27.0 ± 38.1 (24.6 −29.3)	63.4 ± 22.3 (62.0 −64.8)	18.7 ± 27.3 (17.1 −20.4)	72.3 ± 20.8 (71.0 −73.6)
ß-I-HCA	18	51.1 ± 19.9 (49.8 −52.3)	0.57 ± 0.27 (0.55 −0.59)	20.6 ± 37.1 (18.3 −22.9)	81.6 ± 17.2 (80.5 −82.6)	15.9 ± 30.8 (14.0 −17.8)	78.5 ± 14.6 (77.6 −79.4)
ß-HCA	6	71.9 ± 24.0 (70.4 −73.4)	0.73 ± 0.35 (0.71 −0.75)	46.8 ± 48.0 (43.8 −49.8)	97.9 ± 7.0 (97.5–98.4)	45.8 ± 47.7 (42.8 −48.8)	91.4 ± 8.4 (90.9 −91.9)
H-HCA	15	50.8 ± 20.7 (49.6 −52.1)	0.50 ± 0.31 (0.48 −0.52)	20.2 ± 38.8 (17.8 −22.7)	81.4 ± 18.2 (80.3 −82.6)	13.3 ± 28.7 (11.5 −15.1)	82.0 ± 12.4 (81.2 −82.8)

Table 5
Diagnostic performance obtained by the implemented automatic classifiers for the prediction of inflammatory subgroups (I-HCA and ß-I-HCA/binary classification). Classification results are reported after cross-validation (90 % patients training/10 % testing, I-HCA and ß-I-HCA present in both training and testing datasets, 1000 trials with random shuffling) by the Random Forest algorithm. We considered the diagnostic of I-HCA as a "positive case". Top-scores (i.e., highest balanced accuracy) are highlighted in bold characters.

Binary classification of inflammatory types (I-HCA/ß-I-HCA)						
Classifier	Balanced accuracy (%)	AUROC	Sensitivity (%)	Specificity (%)	PPV (%)	NPV (%)
VF model (volume feature)						
T2 no fat saturation	53.3	0.55	56.8	49.9	49.4	42.3
T1 no injection	53.0	0.53	59.2	46.7	49.2	43.2
T1 arterial	51.6	0.51	56.3	47.0	48.2	40.9
T1 portal	52.1	0.53	59.1	45.0	48.3	41.3
ASV model (age, sex and volume features)						
T2 no fat saturation	56.3	0.56	68.3	44.3	53.8	43.4
T1 no injection	55.5	0.54	68.6	42.3	51.7	40.7
T1 arterial	55.1	0.54	66.4	43.8	52.5	41.6
T1 portal	55.3	0.54	67.9	42.6	52.1	41.6
ASVT model (age, sex, volume and texture features)						
T2 no fat saturation	46.6	0.42	61.7	31.5	46.9	29.5
T1 no injection	**73.0**	**0.71**	**85.5**	**60.4**	**69.6**	**65.4**
T1 arterial	43.9	0.41	49.7	38.1	41.8	31.9
T1 portal	44.5	0.33	58.6	30.4	44.9	27.6

Funding

This research did not receive any specific grant from funding agencies in the public, commercial, or not-for-profit sectors.

Guarantor

The scientific guarantor of this publication is Hervé Trillaud.

Statistics and biometry

One of the authors has significant statistical expertise.

Informed consent

Written informed consent was waived by the Institutional Review Board.

Ethical approval

Institutional Review Board approval was obtained (IRB number CRM-2103-143).

No animals subjects used in this study

Study subjects or cohorts overlap

Some study subjects (63 cases) have been previously reported in:

Julien C, Le-Bail B, Touhami K, Frulio N, Adam JF, Laurent C, Balabaud C, Bioulac-Sage P, and Chiche L. Hepatocellular adenoma risk factors of hemorrhage: Size is not the only concern ! Single center retrospective experience of 261 patients. Ann Surg 2021;274 (1):843−50.

Bise S, Frulio N, Hocquelet A, Alberti N, Blanc JF, Laurent C, et al. New MRI features improve subtype classification of hepatocellular adenoma. Eur Radiol 2018; 29(5):2436-2447. doi: 10.1007/s00330-018-5784-5.

Laumonier H, Bioulac-Sage P, Laurent C, Zucman-Rossi J, Balabaud C, Trillaud H. Hepatocellular adenomas: magnetic resonance imaging features as a function of molecular pathological classification. Hepatology 2008;48(3):808-18. doi: 10.1002/hep.22417. Erratum in: Hepatology 2008;48(4):1356.

Methodology

- retrospective
- diagnostic or prognostic study
- performed at one institution

Key points

- Non-invasive subtyping of HCA remains challenging for several subtypes, thus carrying different levels of risks and management; to date, ß-HCA and sh-HCA are not detected and no discrimination between I-HCA and ß-I-HCA is achieved in daily practice.
- Multiple HCA subtyping can be improved using clinical features, i.e., age and sex, combined with MRI-radiomics features.
- Machine-learning algorithms including basic clinical features and MRI-radiomics could help discrimination between I-HCA and ß-I-HCA.

Declaration of competing interest

The authors declare that they have no known competing financial interests or personal relationships that could have appeared to influence the work reported in this paper.

CRediT authorship contribution statement

Guillaume Declaux: Conceptualization, Investigation, Data curation, Writing − original draft. **Baudouin Denis de Senneville:** Supervision, Conceptualization, Methodology, Software, Writing − review & editing, Validation. **Hervé Trillaud:** Supervision, Conceptualization, Investigation, Data curation, Validation, Writing − review & editing. **Paulette Bioulac-Sage:** Data curation, Validation. **Charles Balabaud:** Data curation, Validation. **Jean-Frédéric Blanc:** Data curation, Validation. **Laurent Facq:** Software, Validation. **Nora Frulio:** Investigation, Data curation, Validation, Writing − review & editing.

Acknowledgements

Experiments presented in this paper were carried out using the PlaFRIM experimental testbed, supported by Inria, CNRS (LABRI and IMB), université de Bordeaux, Bordeaux INP and Conseil régional d'Aquitaine (see www.plafrim.fr/).

Supplementary materials

Supplementary material associated with this article can be found, in the online version, at doi:10.1016/j.redii.2024.100046.

References

[1] European Association for the Study of the Liver (EASL). EASL clinical practice guidelines on the management of benign liver tumours. J Hepatol 2016;65(2):38698.
[2] Bunchorntavakul C, Bahirwani R, Drazek D, Soulen MC, Siegelman ES, Furth EE, et al. Clinical features and natural history of hepatocellular adenomas: the impact of obesity. Aliment Pharmacol Ther 2011;34(6):664–74.
[3] Baum JK, Bookstein JJ, Holtz F, Klein EW. Possible association between benign hepatomas and oral contraceptives. Lancet 1973;2(7835):926–9.
[4] Socas L, Zumbado M, Pérez-Luzardo O, Ramos A, Pérez C, Hernández JR, et al. Hepatocellular adenomas associated with anabolic androgenic steroid abuse in bodybuilders: a report of two cases and a review of the literature. Br J Sports Med 2005;39(5):e27.
[5] Bieze M, Phoa SS, Verheij J, van Lienden KP, van Gulik TM. Risk factors for bleeding in hepatocellular adenoma. Br J Surg 2014;101(7):847–55.
[6] Farges O, Ferreira N, Dokmak S, Belghiti J, Bedossa P, Paradis V. Changing trends in malignant transformation of hepatocellular adenoma. Gut 2011;60(1):85–9.
[7] Nault JC, Bioulac−Sage P, Zucman−Rossi J. Hepatocellular benign tumors—From molecular classification to personalized clinical care. Gastroenterology 2013;144(5):888902.
[8] Bioulac-Sage P, Laumonier H, Couchy G, Le Bail B, Sa Cunha A, Rullier A, et al. Hepatocellular adenoma management and phenotypic classification: the Bordeaux experience. Hepatology 2009;50(2):48189.
[9] Bise S, Frulio N, Hocquelet A, Alberti N, Blanc JF, Laurent C, et al. New MRI features improve subtype classification of hepatocellular adenoma. Eur Radiol 2018;29(5):2436–47.
[10] Laumonier H, Bioulac-Sage P, Laurent C, Zucman-Rossi J, Balabaud C, Trillaud H. Hepatocellular adenomas: magnetic resonance imaging features as a function of molecular pathological classification. Hepatology 2008;48(3):808–18 Erratum in: Hepatology. 2008;48(4):1356.
[11] Dourthe C, Julien C, Di Tommaso S, Dupuy JW, Dugot-Senant N, Brochard A, et al. Proteomic profiling of hepatocellular adenomas paves the way to diagnostic and prognostic approaches. Hepatology 2021;74:1595–610.
[12] Van Aalten SM, Thomeer M, Terkivatan T, Dwarkasing R, Verheij J, de Man RD, et al. Hepatocellular adenomas: correlation of MR imaging findings with pathologic subtype classification. Radiology 2011;261(1):172–81.
[13] Reizine E, Ronot M, Ghosn M, Calderaro J, Frulio N, Bioulac-Sage P, et al. Hepatospecific MR contrast agent uptake on hepatobiliary phase can be used as a biomarker of marked β-catenin activation in hepatocellular adenoma. Eur Radiol 2021;31(5):3417–26.
[14] Renzulli M, Clemente A, Tovoli F, Cappabianca S, Bolondi L, Golfieri R. Hepatocellular adenoma: an unsolved diagnostic enigma. World J Gastroenterol 2019;25(20):2442–9.
[15] Julien C, Le-Bail B, Ouazzani Touhami K, Frulio N, Blanc JF, Adam JP, et al. Hepatocellular adenoma risk factors of hemorrhage: size is not the only concern!: single-center retrospective experience of 261 patients. Ann Surg 2021;274(5):843–50.
[16] Nioche C, Orlhac F, Boughdad S, Reuzé S, Goya-Outi J, Robert C, et al. LIFEx: a freeware for radiomic feature calculation in multimodality imaging to accelerate advances in the characterization of tumor heterogeneity. Cancer Res 2018;78(16):4786–9.
[17] Masson I, Da-Ano R, Lucia F, Doré M, Castelli J, Goislard de Monsabert C, et al. Statistical harmonization can improve the development of a multicenter CT-based radiomic model predictive of nonresponse to induction chemotherapy in laryngeal cancers. Med Phys 2021;48(7):4099–109.
[18] Jolliffe IT, Cadima J. Principal component analysis: a review and recent developments. Philos Trans A Math Phys Eng Sci 2016;374(2065):20150202.
[19] Halligan S, Menu Y, Mallett S. Why did European Radiology reject my radiomic biomarker paper? How to correctly evaluate imaging biomarkers in a clinical setting. Eur Radiol 2021;31(12):9361–8.
[20] Kohavi R. A study of cross validation and bootstrap for accuracy estimation and model selection. Morgan Kaufmann; 1995. p. 1137–43.
[21] Cantor SB, Kattan MW. Determining the area under the ROC curve for a binary diagnostic test. Med Decis Making 2000;20(4):468–70.
[22] Jia Y, Cai H, Wang M, Luo Y, Xu L, Dong Z, et al. Diffusion kurtosis MR imaging versus conventional diffusion-weighted imaging for distinguishing hepatocellular carcinoma from benign hepatic nodules. Contrast Media Mol Imaging 2019:2030147.
[23] Ba-Ssalamah A, Antunes C, Feier D, Bastati N, Hodge JC, Stift J, et al. Morphologic and molecular features of hepatocellular adenoma with gadoxetic acid-enhanced MR Imaging. Radiology 2015;277(1):104–13.
[24] Yoneda N, Matsui O, Kitao A, Kozaka K, Gabata T, Sasaki M, et al. Beta-catenin-activated hepatocellular adenoma showing hyperintensity on hepatobiliary-phase gadoxetic-enhanced magnetic resonance imaging and overexpression of OATP8. Jpn J Radiol 2012;30(9):777–82.
[25] Pellat A, Barat M, Coriat R, Soyer P, Dohan A. Artificial intelligence: a review of current applications in hepatocellular carcinoma imaging. Diagn Interv Imaging 2023;104(1):24–36.